APPLIED SCIENCES AND ENGINEERING

Haynes-Shockley experiment analogs in surface and optoelectronics: Tunable surface electric field extracting nearly all photocarriers

Yibo Zhang[1], Sara Almenabawy[1], Nazir P. Kherani[1,2]*

Photocarriers predominantly recombine at semiconductor surfaces and interfaces, assuming high bulk carrier lifetime. Consequently, understanding the extraction of photocarriers via surfaces is critical to optoelectronics. Here, we propose Haynes-Shockley experiment analogs to investigate photocarrier surface extraction. A Schottky junction is used to tune the silicon near-surface electric field strength that varies over several orders of magnitude and simultaneously observe variations in broadband photocarrier extraction. Schottky barrier height and surface potential are both modulated. Work function tunable indium tin oxide (ITO) is developed to precisely regulate the barrier height and collect photocarriers at 0 V bias, thus avoiding the photocurrent gain effect. All experiments demonstrate >98% broadband internal quantum efficiency. The experiments are further extended to wave interference photonic crystals and random pyramids, paving a way to estimate the photogeneration rate of diverse surface light-trapping topologies by collecting nearly all photocarriers. The insights reported here provide a systematic experimental basis to investigate interfacial effects on photocarrier spatial generation and collection.

INTRODUCTION

Semiconductor band-to-band transitions and the corresponding photocarrier generation and extraction are fundamental processes for a wide range of optoelectronic applications, such as photocatalysis (1–3), photovoltaics (4–7), photodetection (8–15), and optical communications (16–19). For a semiconductor with high bulk crystal quality and minimal-to-negligible bulk radiative/nonradiative recombination processes, the loss of photocarriers to surface recombination is the most important barrier to attaining high-performance optoelectronic devices (12, 20, 21). For example, a typical commercial Si wafer has hundreds of micrometer diffusion length for minority carriers. This suggests that the generated photocarriers, under low optical injection, have a negligible recombination rate in both the diffusion region (presuming a moderate majority carrier doping level) and the space charge region (where background concentrations for both electrons and holes are low). Accordingly, these photocarriers mostly recombine at the Si interface, assuming the absence of a heavily doped region that would otherwise enhance Auger recombination (20, 21). On the other hand, semiconductor or dielectric surfaces/interfaces have been regarded as ambiguous systems for many decades, including interfaces with the mature material of Si, due to a multiplicity of factors. One reason is the termination of periodic/nonperiodic bonds at the surface, arising from nano/microfabrication processing. Another influential factor is the chemical reactions with various elements resulting in a heterogeneous interface that collectively introduces a wide range of surface defect energy levels within the forbidden band (22, 23). To minimize the effect of surface recombination, passivation technologies have been developed principally in two forms: chemical passivation and field passivation. Chemical passivation reduces the surface defect states by saturating the dangling bonds (20, 21, 24–28). Field passivation, in contrast, creates a surface electric field via fixed charges within the adjoining dielectric films. This field effect repels one type of carrier at the surface, which in turn reduces the surface recombination rate with the other carrier —in essence, the induced field effect pushes the near-surface region into depletion or inversion (12, 29). For practical optoelectronic heterojunction devices, such as photodetectors and solar cells, surface band bending induced by energy band offsets of two contact materials with dissimilar work functions usually leads to a certain level of field passivation (30–36). This field effect, together with a low density of surface defect states (realized by chemical passivation), contributes to the realization of ultralow photocarrier surface recombination and thus ultrahigh performance optoelectronic devices.

The ultimate objective of these passivation technologies is to enable complete extraction of the photocarriers approaching the surface. While much research has been carried out to develop passivation technologies and correspondingly high-performance optoelectronic devices, there is limited reporting of theoretical and experimental studies that directly observe the relationship between photocarrier extraction and the strength of the near-surface electric field. Moreover, commonly reported passivation/extraction technologies assume a constant surface recombination velocity for all photocarriers approaching the surface (24). However, the optical generation profile within a given absorber varies with the wavelength of the incident light. Hence, the requirements for collecting photocarriers generated at different locations, which are dictated by the semiconductor absorption properties and the light-trapping designs, are not all "equal" for achieving the ideal 100% quantum efficiency. Establishing a deeper experimental understanding of the influence of the near-surface electric field on broadband photocarrier collection for the range of possible light-trapping

[1]The Edward S. Rogers Sr. Department of Electrical and Computer Engineering, University of Toronto, 10 King's College Road, Toronto, ON M5S 3G4, Canada. [2]Department of Materials Science and Engineering, University of Toronto, 184 College Street, Toronto, ON M5S 3E4, Canada.
*Corresponding author. Email: nazir.kherani@utoronto.ca

surface topologies is essential for the development of optimal opto-electronics—a research area that has remained largely unexplored.

The Haynes-Shockley experiment—a classic experiment in semiconductor physics—uses two contacts on a semiconductor to measure the signal delay between carrier injection and carrier collection by which it determines the carrier mobility and lifetime (37). The soul of the Haynes-Shockley experiment is minority carrier generation at one location and collection at some other position, wherein the electric field is applied across the entire semiconductor to mitigate the carrier diffusion process in drift-dominated charge transport (37). In this work, we propose and demonstrate analogs of the Haynes-Shockley experiment to develop insight into the influence of the surface electric field on broadband photocarrier extraction. Two asymmetrical contacts are configured on n-Si. Broadband minority photocarriers are generated at different locations within the Si absorber and then collected at the surface under the influence of various electric potential profiles. A series of proof-of-concept Schottky junction devices with tunable surface electric field strengths are proposed. Near-surface electric field strengths ranging from 10^4 to 10^6 V/m are explored to directly observe the broadband photocarrier recombination and collection. In all devices, no special chemical passivation process is implemented to solely investigate the field effect on photocarrier collection. More than ~98% broadband internal quantum efficiency (IQE) is demonstrated, providing essential insights in the design and realization of high quantum efficiency in various optoelectronic devices.

Important photocarrier surface extraction phenomena are observed with tunable surface electric field. (i) For devices with a narrow surface band bending (<1 μm depletion region width), it is consistently demonstrated that a sufficiently high surface potential and the correspondingly strong surface electric field (of the order of 10^6 V/m) can extract nearly all photocarriers approaching the surface. It is also observed that photocarriers generated outside of the depletion region have a constant collection rate when they enter the surface. (ii) For devices with a wide depletion region (tens of micrometers width) and a weak surface electric field (10^4 to 10^5 V/m), broadband photocarriers are generated at locations with an electric potential gradient. It is observed that photocarriers generated at the high electric potential region are preferably collected by the surface. This indicates that the particle's high kinetic energy, that is, the high perpendicular-to-surface carrier velocity, is a key reason that approaching-the-surface photocarriers can overcome the trap-assisted recombination process to be fully collected.

Furthermore, the demonstrated experimental results provide a potential method to directly estimate the photogeneration rate for various surface light-trapping topologies. Specifically, it has been widely recognized that many factors, such as the presence of a metallic back reflector and the initial doping of the semiconductor, can cause a substantial parasitic absorption, resulting in an overestimation of the real photogeneration as determined by optical absorption measurements. Hence, obtaining the photogeneration rate for a given semiconductor absorber is a basic yet critical problem. Here, we propose to resolve this challenging problem by collecting nearly all photocarriers for a balanced estimation of the photogeneration in an arbitrary absorber. The present research provides a general framework for photocarrier generation/extraction in semiconductor optoelectronic materials and devices.

RESULTS
Experimental mechanisms
The experimental design is illustrated in Fig. 1. The light beam traverses through a mechanical chopper and a monochromator (Fig. 1A), thereby modulating the source frequency and wavelength of the output beam. The resulting light beam at a given (single) wavelength is focused on the active region of the test devices. Two probes are brought in contact with the indium tin oxide (ITO) and Al contact regions to record the amplitude of the photovoltage between the two contacts as well as the photocurrent. The recorded signal frequency corresponds to the chopper frequency as facilitated by a lock-in amplifier.

Three different types of test devices and their corresponding energy band diagrams at thermal equilibrium are presented in Fig. 1B. The first set of devices (Fig. 1Bi) achieves Schottky barrier height tunability by varying the work function of the ITO thin films. The ITO work function is altered by changing the O_2 to Ar flow ratio during the sputter deposition of the thin film. The Schottky barrier height, as labeled in the energy band diagram, is thus varied to realize a tunable surface potential and correspondingly tunable near-surface electric field. A 3 ohm·cm resistivity (~1.5×10^{15} cm^{-3} doping concentration) n-Si wafer is used to ensure that the depletion region width is within ~1 μm (as simulated below). The near-surface electric field and the electric potential are the principal factors that influence photocarrier recombination and collection, for several reasons. Most of the photocarriers generated by incident photons below 700-nm wavelength are within 10 μm of the top collecting surface. Both Auger recombination and bulk Shockley-Read-Hall (SRH) recombination processes are negligible, due to the elimination of a highly doped region (i.e., dopant-free contact device). The photocarriers generated beyond 10 μm are at depths within their typical diffusion length (hundreds of micrometers) in relation to the collecting surface. No voltage bias is applied during the optoelectrical testing of these devices. This set of devices has a strong surface electric field of the order of ~10^6 V/m. The significance of this experiment is to fully mitigate the photocurrent gain effect by tuning the work function of the contact material and collecting photocarriers without any external bias. As demonstrated below, the optical injection for all devices with various Schottky barrier heights is nearly constant. Furthermore, the strategies use limited surface chemical passivation effect for test devices, making it possible to consistently observe the sole influence of the surface electric field on photocarrier extraction.

The second set of devices (Fig. 1Bii) has a fixed work function ITO contact, sputter-deposited with only Ar (no O_2 flow) onto 3 and 0.3 ohm·cm (~1.9×10^{16} cm^{-3} doping level) resistivity n-Si wafers. In this case, the Schottky barrier height is fixed (see the related energy band diagram), and the near-surface electric field is modulated by applying an external voltage bias. The surface depletion region for these devices is also within ~1 μm width under a small bias, while the surface potential is variable to realize a tunable near-surface electric field under an external voltage bias. The surface electric field strength is at the order of 10^6 V/m, and a slight photocurrent gain effect is exhibited in this case. The purpose of this set of devices is to compare their photocarrier extraction with the "no-photocurrent-gain" devices in Fig. 1Bi, as well as to compare their performance with the following "weak-surface-field" devices (the third set).
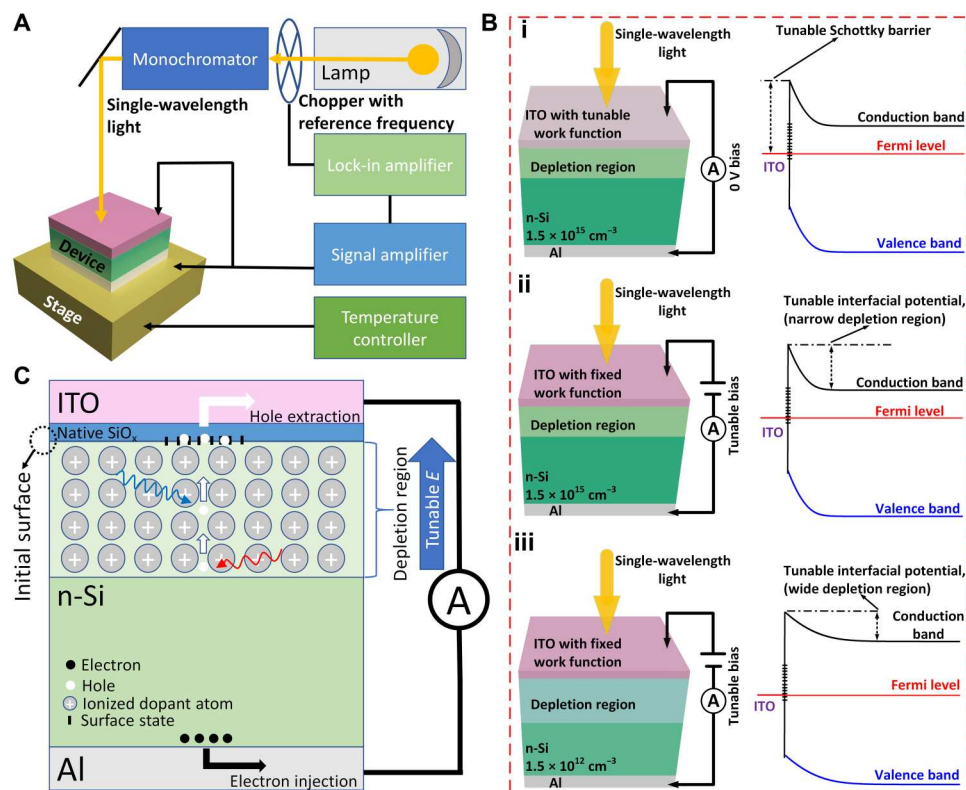
Fig. 1. Experimental apparatus and device configurations. (**A**) Optoelectronic test apparatus for devices where the near-surface electric field strength is varied. (**B**) Device configurations and the corresponding energy band diagrams at thermal equilibrium illustrating the various mechanisms by which the near-surface electric field strength is tuned. (i) Tunable Schottky barrier height via changes in the ITO work function with the device measured at zero bias. (ii) Tunable external bias on devices with a narrow depletion region. (iii) Tunable external bias on devices with a wide depletion region. (**C**) Cross-sectional diagram illustrating the device operation under illumination; absorption of photons of different wavelengths in the depletion region is schematically represented in blue and red.

The first two sets of devices can be viewed as analogs of the carrier diffusion case in the Haynes-Shockley experiment, wherein, without an applied bulk electric field, minority carriers undergo a diffusion-dominated process with generation occurring at different locations and collection at one point (*37*). In our experiments, most of the photocarriers due to wavelengths of 500 to 900 nm are generated within the electrically neutral region (i.e., they are mostly generated outside of the narrow depletion region, given the absorption depth of Si). Accordingly, these photocarriers undergo diffusion-dominated transport before they enter the surface depletion region.

The third set of devices (Fig. 1Biii) is designed by depositing a fixed work function ITO thin film onto high-resistivity Si (3000 ohm·cm, $\sim 1.5 \times 10^{12}$ cm^{-3} doping level). The lower doping level results in a wider depletion region (tens of micrometers width, as simulated below) in silicon and a lower order of magnitude of the peak near-surface electric field value (10^4 to 10^5 V/m, as simulated below). In this condition, even with a high applied voltage of up to a few volts, the near-surface electric field is still below the order of $\sim 10^6$ V/m, making it possible to clearly observe the broadband photocarrier extraction as a function of the surface electric field strength spanning orders of magnitude. The third set of devices can be viewed as an analog of the carrier drift case in the Haynes-Shockley experiment, wherein, under an applied bulk electric field, drift-dominated carrier transport is used to determine the carrier mobility by changing the distance between the carrier injection and collection positions (*37*). In our experiment, most of the photocarriers associated with wavelengths of 300 to 1000 nm are generated at different locations within the wide depletion region. Hence, the photocarriers generated at different positions have different potential energies and undergo drift-dominated transport before being collected at the surface.

Device operation under illumination is illustrated in Fig. 1C. Under illumination, photons are absorbed by the silicon lattice leading to the band-to-band transition that results in photogenerated carriers. Because of upward band bending at the ITO/n-Si interface, the minority photogenerated holes transport toward the top surface contact where they are collected as an external photocurrent, while the rear-side ohmic contact enables the majority electron injection between n-Si and Al. The Al/n-Si contact in this work is not intentionally optimized for low contact resistance to avoid additional treatments that may influence the distribution of the initial Si surface states. Note that Al, with a work function of ~4.2 eV, is deemed to form an unoptimized ohmic contact with n-Si; various strategies involving insertion of ultralow work function interfacial layers between Al and n-Si have been reported to improve the contact quality (*38–40*). However, for low optical injection optoelectrical tests in this work, it is shown below that the unoptimized Al/n-Si ohmic contact provides adequate performance on majority carrier injection.

For all devices, the depletion region, wherein the dopant atoms are ionized, is adjusted to tune the near-surface electric field strength and the overall surface potential for effective photocarrier collection. This is schematically illustrated by the absorption of blue- and red-labeled photons in Fig. 1C. Furthermore, as shown in Fig. 1C, the initial Si surface (where the native oxide on the Si surface is left unaltered) is intentionally unchanged for all samples so as not to introduce chemical passivation processes that would modify the initial Si interface states, thereby solely investigating the field effect on photocarrier collection. Nevertheless, it is acknowledged that the deposition process and/or the surface electric field effects may unavoidably lead to a redistribution of the surface states.

Thin-film characterization

Fundamental ITO thin-film properties and surface photovoltage (SPV) of the heterojunctions are presented in Fig. 2. The ultraviolet photoelectron spectroscopy (UPS) results over the energy cutoff edge region are shown in Fig. 2A. ITO thin films were deposited on quartz substrates with various O_2:Ar flow rates during sputtering. The full energy scale UPS results and cutoff energy edge fitting details are given in fig. S1. With an increasing O_2 flow ratio, a small work function shift is observed. On the basis of the fitting process in fig. S1B, the sputtered ITO thin film with a higher O_2 flow ratio has a lower cutoff energy and a higher work function. Specifically, the ITO thin film at 1.2% O_2 flow has the highest work function,

which is ~0.5, ~0.43, and ~0.13 eV higher than that at 0.2% O_2, at 0.4% O_2, and at 1% O_2, respectively. This excellent tunability of the ITO work function enables precise control of the device Schottky barrier, as shown in Fig. 1Bi. ITO is a highly degenerate n-type semiconductor, for which the Fermi level lies within the conduction band, indicative of the work function. Two major mechanisms contribute to the ITO conductivity: The initial oxygen vacancies and the Sn^{4+} coupling to indium oxide lattice can both release free electrons as mobile charges in the ITO conduction band. The oxygen vacancies have been regarded as an important donor that increases the electron concentration for ITO thin films and many other transparent conductive oxides (41, 42). Specifically, with a constant Sn doping ratio, the oxygen vacancies dominate the electron concentration within ITO thin film (41). In this work, a slight O_2 gas flow during the sputtering process reduces the oxygen vacancies in ITO, thus reducing the free electron concentration in the ITO conduction band and increasing the ITO work function. Some treatments such as O_2 plasma and O_2 flow during ITO sputtering have been reported to increase the ITO work function (43–45). It has also been reported that O_2 flow during sputtering enables a low-conductivity nanometer-thin ITO film for transistor applications (46).

Optical transmission, surface roughness, and energy-dispersive x-ray spectroscopy (EDS) mappings results of the ITO thin films are respectively measured in figs. S2 to S4. The absorption of the ITO/n-Si/Al structure is presented in Fig. 2B. It is seen that ITO/n-Si shows a typical destructive interference property for the incident light
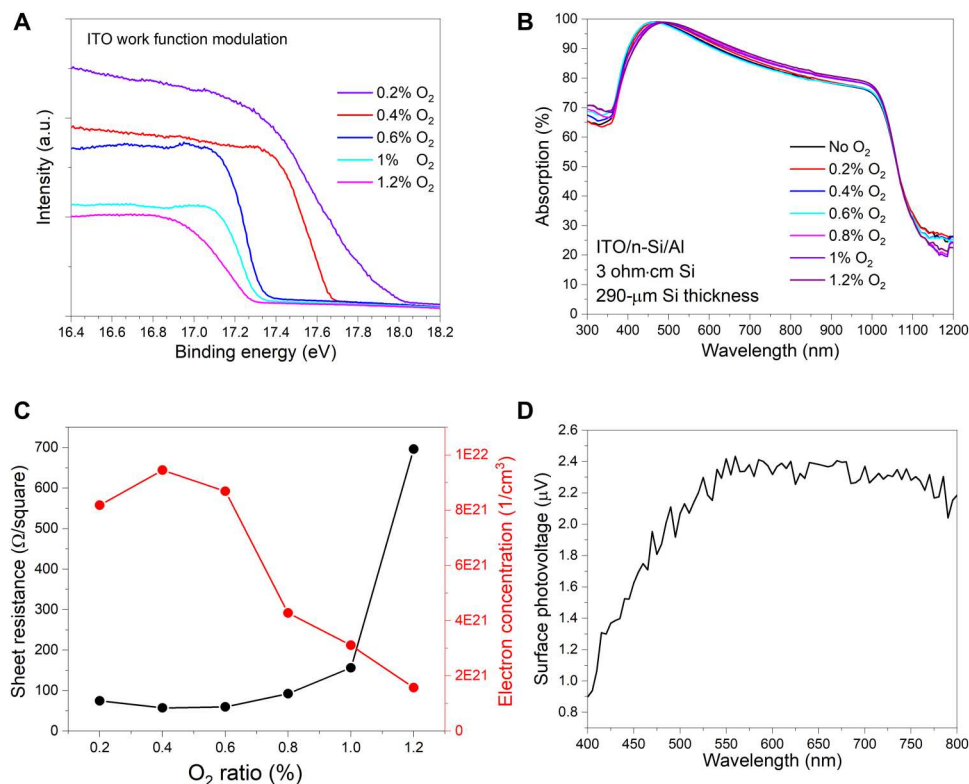
Fig. 2. Characterization of the ITO thin films and ITO/n-Si/Al heterojunctions. (**A**) Ultraviolet photoelectron spectroscopy (UPS) results for ITO thin films deposited with various O_2:Ar ratios to determine the cutoff energy edge. a.u., arbitrary units. (**B**) Optical absorption of ITO/n-Si/Al structures, with varying O_2 concentrations in Ar during ITO sputtering. (**C**) Sheet resistance and carrier concentration for ITO thin films determined by Hall effect measurement, as a function of O_2 flow ratio. (**D**) SPV measurement of ITO/n-Si/Al under illumination over a wavelength range of 400 to 800 nm.

from ~460- to ~480-nm wavelengths, making it possible for nearly complete optical absorption within Si absorber at a certain wavelength, and hence demonstration of the nearly complete photocarrier extraction. A zoomed-in image of Fig. 2B is plotted in fig. S5, showing ~99% peak absorption for all samples. The optical generation for all the samples with various O_2 flows is almost constant, ensuring a negligible change in the optical injection level for the following optoelectrical test. The sheet resistance and the carrier concentration for ITO thin films are measured by the Hall effect in Fig. 2C. With an increase in the O_2 flow ratio, the overall sheet resistance increases, while the carrier concentration decreases. This is consistent with the UPS results shown in Fig. 2A: For a higher O_2 flow ratio, the reduction of the oxygen vacancies leads to a lower free electron concentration, thus contributing to a slight increase in the ITO work function. With a 1.2% O_2 ratio, the ITO thin film exhibits ~700 ohms/square sheet resistance and ~1.9×10^{21} cm^{-3} electron concentration. The SPV measurement, shown in Fig. 2D, is for a device made of an ITO thin film with a 1.2% O_2 flow. For the low optical injection case, the near-surface potential change (of the order of microvolts) is far lower than the built-in surface potential of the device, indicating that the near-surface electric field can be considered to be unchanged under weak illumination.

Planar Si device performance under dark

The planar Si device performance under dark is analyzed in Fig. 3. The current density-voltage (J-V) curves for devices with various O_2 flow ratios during ITO sputtering are measured in Fig. 3A. All devices show a typical current rectification property, where the reverse dark current is markedly lower than the forward current. For example, rectification ratios (defined as the ratio of the forward current to reverse current) of ~0.72×10^3 and ~1.52×10^3 are respectively observed for devices with 1% O_2 and 1.2% O_2 at ±0.5 V. This suggests that the electrons from ITO need to overcome an energy barrier to be injected into n-Si under reverse bias, thus revealing the existence of a Schottky barrier from ITO to n-Si. Furthermore, a dramatic decrease in both the forward and reverse current densities is exhibited with increasing O_2 flow ratio. This is explained by the following equation

$$J = J_0 \left\{ \exp\left[\frac{q(V - IR)}{nkT} \right] - 1 \right\} \quad (1)$$

where q is the electric charge, V is the applied voltage, I is the current, R is the series resistance, n is the ideality factor, T is the temperature, k is the Boltzmann constant, and J_0 is the reverse saturation current density. J_0 is expressed as follows

$$J_0 = A^* T^2 \exp(-\Phi_B/kT) \quad (2)$$

where A^* is the Richardson constant for n-Si and Φ_B is the Schottky barrier height. The higher work function of ITO thin films with higher O_2 flow ratios enhances the Schottky barrier height and consequently reduces the dark current density, as indicated in Eq. 2. Meanwhile, the reduced conductivity of ITO thin films, as shown in Fig. 2C, increases the entire series resistance R of the diode, thus explaining the drop of the forward current density as expressed in Eq. 1.

The high reverse dark current density of 10^{-4} A/cm^2 for devices with a 0.2% O_2 flow suggests that the low-quality native oxide has a negligible influence on reducing the device reverse current. In addition, the device performance is influenced by both the trap-assisted tunneling process (by surface states) and energy band alignment of tunable work function ITO contact and n-Si. This is further confirmed by the change in Schottky barrier height as a function of O_2 flow shown in Fig. 3B. The Schottky barrier heights for all devices are extracted in fig. S6 by fitting the forward J-V curve using the Cheung's method (47). As the O_2 flow ratio increases from 0.2 to 1.2%, the Schottky barrier height and the series resistance increase from ~0.6512 to ~0.7845 eV and from ~202.2 to ~356.4 ohms, respectively. The barrier height for devices with 1.2% O_2 flow is ~0.1333 eV higher than that for devices with 0.2% O_2 flow, suggesting that the tunable ITO work function modulates the device barrier height. This ~0.1333 eV barrier height shift is not consistent with the ITO work function change (~0.5 eV from 0.2% O_2 to 1.2% O_2 in Fig. 2A), further confirming that the contact potential difference and surface states together influence the device performance. Note that the presence of surface states and the related Fermi level pinning effect may be a reason that prevents a consistent change between the ITO work function and the device Schottky barrier height. In the presence of surface states, the surface potential change drops in both the interfacial region and the depletion region. The interfacial states share in the electric potential drop induced by the tunable work function of the ITO thin films, thus hindering further depletion of the bulk Si. It is worth mentioning that the surface Fermi level is not totally pinned since the tunable ITO work function can still modulate the Schottky barrier height as shown in Fig. 3 (A and B). It is also suggested that the work function determined from UPS measurements is highly related to the surface of the tested samples and, accordingly, may vary slightly with the actual interfacial contact region, thus failing to precisely provide performance prediction for practical devices. Nevertheless, the obtained J-V curves reflect the energy band alignment and the changes in Schottky barrier heights.

The surface state distribution for devices made with 1.2% O_2 flow ITO films is calculated in Fig. 3C. The calculation process is shown in the Supplementary Materials, and the method can be found elsewhere (48, 49). The surface defect density is simulated to range from ~10^{13} to ~10^{14} eV^{-1} cm^{-2}. The energy level of the surface states E_{ss} mainly occupies the region from ~0.4 to ~0.9 eV above the top of the valence band E_v. The surface state distribution for devices made with 0.4% O_2 is calculated in fig. S7. Compared with a well chemically passivated surface with a defect level below the order of ~10^{12} eV^{-1} cm^{-2} (50), we conclude that the change in the O_2 flow ratio during ITO sputtering leads to a limited surface chemical passivation effect. The dark current density for devices made on the low-resistivity wafers (3 and 0.3 ohm·cm) and high-resistivity wafers (3000 ohm·cm) is measured in Fig. 3D. There was no O_2 flow during ITO thin-film deposition for these devices. For all devices, a similar current rectification property is observed, indicating that ITO forms a typical Schottky contact with variously doped Si in this work. The barrier heights are simulated to be ~0.6811, ~0.6182, and ~0.6750 eV for devices made on 0.3 ohm·cm n-Si, 3 ohm·cm n-Si, and 3000 ohm·cm n-Si, respectively. The linear scale J-V curve for the 3 ohm·cm device is plotted in fig. S8: The high forward current density suggests that there is sufficiently high electron injection from Al to n-Si, showing that Al forms an ohmic contact with n-Si.

The capacitance-voltage (C-V) properties at various frequencies for the 3 ohm·cm n-Si device are shown in Fig. 3E. The junction
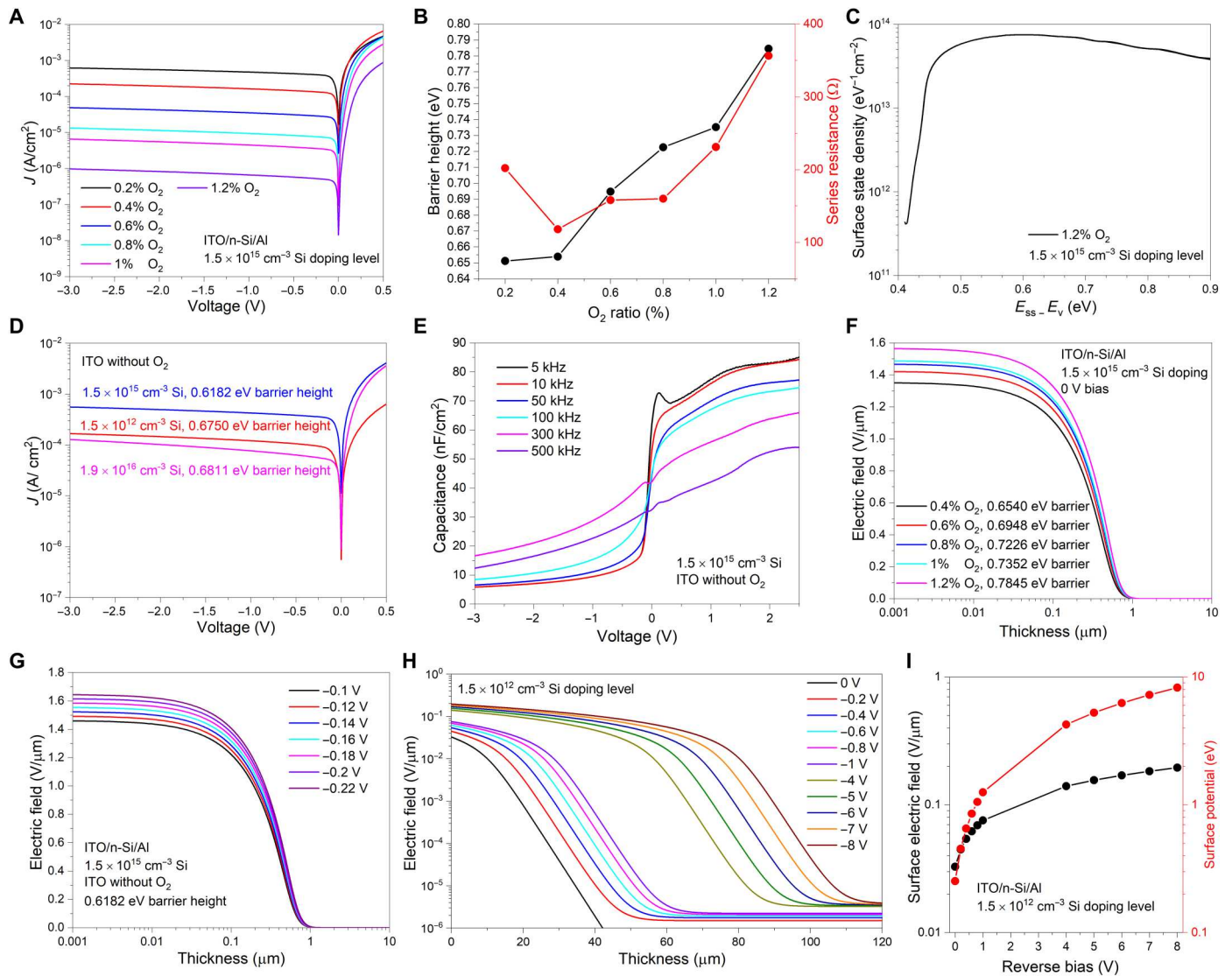
Fig. 3. Planar Si device performance. (**A**) Dark current density for devices with various O_2 flows during ITO thin-film deposition. (**B**) Extracted Schottky barrier height and series resistance for devices with various O_2 flows. (**C**) Calculated surface state density distribution. (**D**) Dark current density for devices with three different resistivities: 0.3 ohm·cm (1.9×10^{16} cm^{-3} doping concentration), 3 ohm·cm (1.5×10^{15} cm^{-3} doping concentration), and 3000 ohm·cm (1.5×10^{12} cm^{-3} doping concentration). For all devices, ITO was deposited without O_2 flow during sputtering. (**E**) Capacitance-voltage measurement under different frequencies (3 ohm·cm device, ITO thin film without O_2 flow). (**F**) Simulated electric field distribution at 0 V bias for devices with different Schottky barrier heights. (**G**) Simulated electric field distribution as a function of applied reverse voltage bias (3 ohm·cm device, ITO thin film without O_2 flow). (**H**) Simulated electric field distribution as a function of applied reverse voltage bias (3000 ohm·cm device, ITO thin film without O_2 flow). (**I**) Extracted near-surface electric field and the overall surface potential as a function of reverse bias (3000 ohm·cm device, ITO thin film without O_2 flow).

capacitance is determined by the overall electric charge change under an applied time-varying voltage. Under forward bias, a capacitance peak is observed at ~0.12 V at a low frequency of 5 kHz; this peak disappears at higher frequencies. This reveals the presence of surface states; we note that similar observations have been reported for low-frequency C-V measurements (51–54). The surface defect states have been reported to own a large time constant (51, 52). Under low frequencies, the large time constant means that the charge capture and emission processes of these surface states can keep up with the change in the applied voltage. The overall capacitance change is then determined by the rate of charge transfers

within both the depletion region and the interfacial states, causing a capacitance peak at 5 kHz. The forward voltage bias corresponding to this peak is closely related to the relative position between these surface states and the surface valence band (51). At higher frequencies, this peak disappears since the surface states cannot respond to the fast change in the voltage signal; hence, the capacitance is principally determined by the charge change within the depletion region. A detailed mathematic description is given in the Supplementary Materials to illustrate the C-V curves. The C-V results measured for samples with 1.5×10^{12} cm^{-3} Si doping level are given in fig. S9.

The one-dimensional (1D) electric field distribution for the above devices is simulated in Fig. 3 (F to H), by solving Poisson's equation

$$-\frac{d^2\psi_B}{dx^2} = \frac{dE}{dx} = \frac{\rho}{\varepsilon_{si}} \qquad (3)$$

where ψ_B is the electric potential in the depletion region, x is the length, E is the electric field, ρ is the overall charge concentration, and ε_{si} is the permittivity of Si. The electric field distribution for devices with various barrier heights (devices in Fig. 3A) is simulated in Fig. 3F. According to Eq. 3, a larger Schottky barrier indicates greater surface band bending (i.e., larger surface potential) and correspondingly larger near-surface electric field. The peak of the near-surface electric field gradually increases with increasing Schottky barrier height. The depletion region is simulated to be ~1 μm width. For the device with a 1.2% O_2 flow ITO thin film (~0.7845 eV barrier height), the near-surface electric field is ~1.58 V/μm with a ~0.5378 eV built-in potential. In addition, the surface field strength and built-in potential are respectively ~1.3479 V/μm and ~0.4045 eV for the 0.2% O_2 ITO device with a ~0.6512 eV Schottky barrier. The electric field distribution is simulated at various applied reverse voltages, as shown in Fig. 3G, for a device with ~3 ohm·cm resistivity and ~0.6182 eV barrier height (device in Fig. 3D). As indicated, the surface depletion region width is about ~1 μm at small reverse bias from −0.1 to −0.22 V. At −0.18 V and −0.2 V bias, the near-surface electric field is ~1.59 and ~1.62 V/μm, respectively, and the built-in potential is ~0.5515 and ~0.5715 eV, respectively.

The electric field for the devices made on high-resistivity Si (3000 ohm·cm, ~0.6750 eV barrier height in Fig. 3D) is simulated in Fig. 3H. The lowest surface electric field (10^4 to 10^5 V/m) and the widest depletion region (tens of micrometers) are simulated for this set of devices, under bias ranging from 0 to −8 V. For these high-resistivity Si devices, a very weak electric field of the order of 1 V/m extends over hundreds of micrometers in depth. Specifically, when the high bulk resistance cannot be ignored compared with the depletion region's resistance, the applied voltage will drop in both the depletion region and the bulk region, leading to a weak electric field extending into the bulk region. The near-surface electric field and the corresponding surface potential for 3000 ohm·cm devices are summarized in Fig. 3I as a function of reverse voltage bias. For this set of devices, the surface electric field strength is still below the order of 10^6 V/m even at high reverse bias of up to −8 V. Furthermore, there is also a large range of surface potential change from ~0.25 eV (at thermal equilibrium without any bias) to ~8.25 eV (at −8 V bias, assuming that all of the applied bias drops in the depletion region). The electric field distribution for a device made on 0.3 ohm·cm (1.9×10^{16} cm^{-3} doping level) n-Si is simulated in fig. S10. The surface electric field and the built-in potential for other devices are summarized in fig. S11.
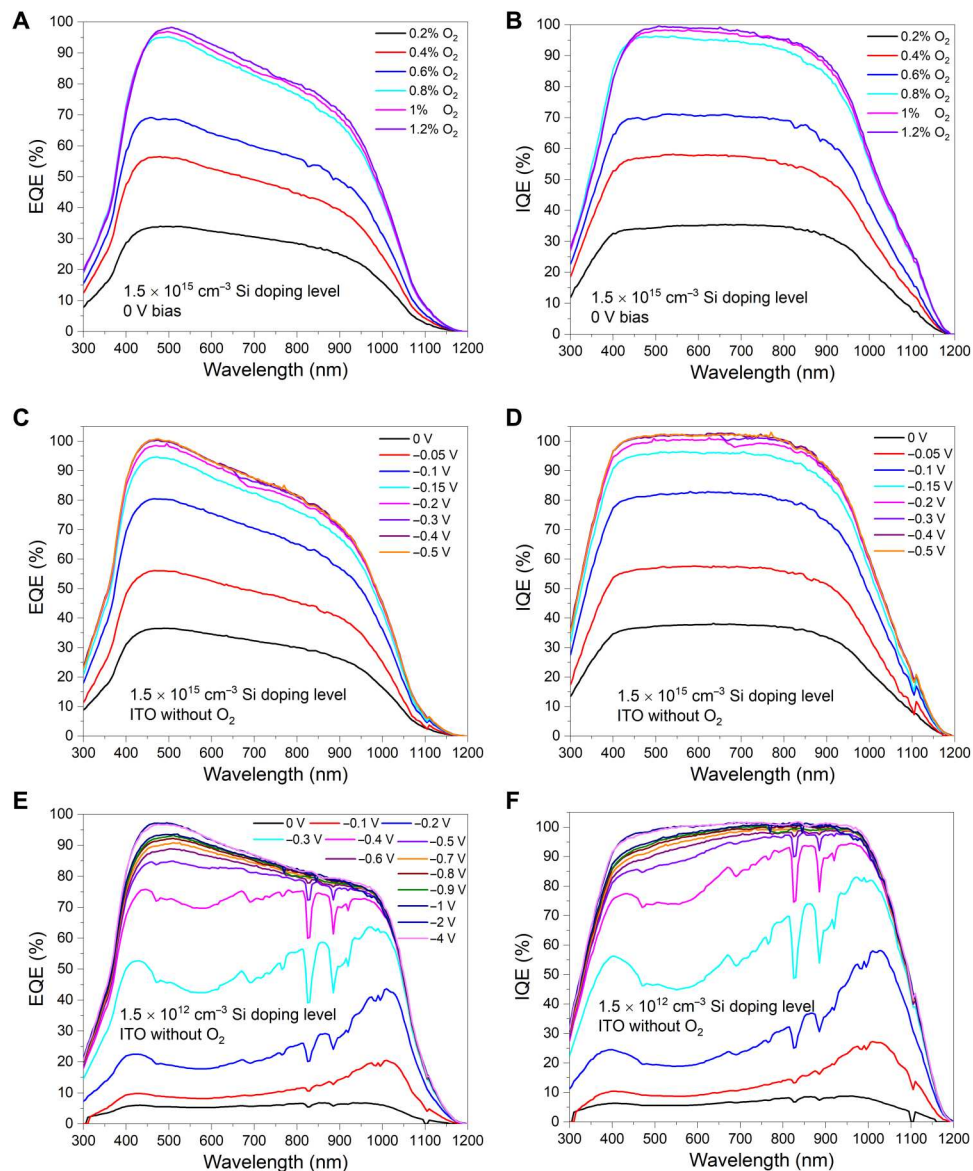
Quantum efficiency for planar Si devices

The quantum efficiency is investigated in Fig. 4. External quantum efficiency (EQE) is the ratio of collected photocarriers to incident photons. Specifically, 100% EQE means that all incident photons are absorbed and converted to photocarriers without recombination loss (namely, every absorbed photon produces one electron-hole pair). IQE is defined as the ratio of the collected photocarriers

to absorbed photons. Similarly, 100% IQE indicates that all absorbed photons are converted to photocarriers (that is, the absorption is not necessarily 100%). The EQEs for devices with varying O_2 flows during ITO deposition are illustrated in Fig. 4A. With increasing Schottky barrier height, the EQE gradually saturates at its peak value. The measurement is performed at 0 V bias to ensure no photoconductive gain effect (55). The EQE of ITO (1.2% O_2)/n-Si peaks at 465-nm wavelength with a value of greater than ~99%. Considering that the absorption rate varies with each wavelength, a peak of ~99% EQE at a certain wavelength indicates that there is almost negligible surface recombination for the corresponding photogenerated carriers that reach the surface region. Furthermore, these samples have a "normal" surface state density level of the order of ~10^{13} to ~10^{14} eV^{-1} cm^{-2}, as simulated in Fig. 3C, showing limited chemical passivation effects due to the ITO thin films. Therefore, the saturation of the quantum efficiency indicates that at a sufficiently high surface potential and the correspondingly high near-surface electric field, photocarriers can overcome the trap-assisted recombination effect of the surface, thereby being collected with negligible recombination loss. Also, the optical injection is small, and thus, the associated near-surface potential change for each wavelength of illumination is negligible compared to the large built-in potential at thermal equilibrium, as shown by the SPV measurements in Fig. 2D. Specifically, the quantum efficiency saturates with the ITO thin film deposited with a 1.2% O_2 ratio (corresponding to ~0.7845 eV barrier height, ~1.58×10^6 V/m near-surface electric field, and ~0.5378 eV built-in potential, as shown in fig. S11A). The IQE of the device is calculated in Fig. 4B, by the following equation

$$\text{IQE} = 100\% \times \text{EQE}/\text{Absorption} \qquad (4)$$

where the absorption is taken from Fig. 2B. The low IQE at a low barrier height (for example, ~34% IQE from 450 to 850 nm for the 0.2% O_2 flow ITO–based device) indicates that most photocarriers recombine at the silicon surface before contributing to the photocurrent. For the 1.2% O_2 flow ITO–based device, a near-unity IQE over a broadband spectrum is observed (more than ~99% from 500 to 570 nm and more than ~97% from 455 to 730 nm). This is consistent with the conclusion that almost all the photocarriers approaching the surface are collected. The high peak EQE exceeding ~99% and high broadband IQE over ~98% suggest that, under low optical injection, the unoptimized backside ohmic contact is adequate and enables sufficient majority electron injection from n-Si to Al. The IQE loss at short wavelengths is due to the ultraviolet (UV) light parasitic absorption of the ITO thin film, while the loss at long wavelengths is due to the rear-side photocarrier recombination in the absence of a back surface field as well as the free-carrier absorption in Al.

The quantum efficiency at different applied reverse voltages is measured in Fig. 4C. The ITO contact is sputtered without O_2 flow [the test device has a ~0.6182 eV Schottky barrier height, shown in Fig. 3 (D and G)]. The quantum efficiency starts to saturate when the applied voltage reaches ~−0.18 to ~−0.2 V. The peak quantum efficiency exceeds 100% as the applied voltage increases up to ~−0.5 V, corresponding to an IQE above unity over a broadband of the spectrum, as shown in Fig. 4D. This is due to the photoconductive gain effect, in which the electrons from the ITO thin-film tunnel into n-Si through the surface defects and recombine

Fig. 4. Quantum efficiency characterization of planar Si devices. (**A**) External quantum efficiency (EQE) for devices with various O_2 flow ratios during ITO sputtering (3 ohm·cm wafer, 1.5×10^{15} cm^{-3} doping concentration, 0 V bias). (**B**) IQE calculated from (A). (**C**) EQE for devices with a fixed Schottky barrier height (3 ohm·cm wafer, no O_2 flow during ITO sputtering) under different applied reverse biases. (**D**) IQE calculated from (C). (**E**) EQE for devices made on high-resistivity Si (3000 ohm·cm, 1.5×10^{12} cm^{-3} doping concentration, no O_2 flow during ITO sputtering) under different applied reverse biases. (**F**) IQE calculated from (E). (E) and (F) have the same figure legend.

with the photogenerated holes. This enables the photocarrier recycling effect before the final recombination of the photogenerated holes, hence leading to a quantum efficiency above unity. It is observed that the photocurrent saturates under ~−0.2 V bias, corresponding to ~1.62 V/μm near-surface electric fields, and ~0.5715 eV surface potentials, as shown in fig. S11B. This is in excellent agreement with the tunable barrier height results at 0 V bias shown in Fig. 4 (A and B), where the photocurrent saturates at ~1.58 V/μm near-surface electric field and ~0.54 eV built-in potential. This consistent observation suggests that for a surface with a certain state density distribution (i.e., without intentional chemical passivation), sole constantly high surface potential and strong

surface electric field are sufficient to extract nearly all photocarriers approaching the surface, and the strength value of this field/potential is nearly constant for the initial surface.

Photocarrier recombination investigated under lower surface electric field in the range of 10^4 to 10^5 V/m is shown in Fig. 4 (E and F). We examine the case of a widely distributed built-in potential by using a high-resistivity wafer (3000 ohm·cm n-Si, simulated in Fig. 3H). The optical absorption for the ITO-coated high-resistivity Si is given in fig. S12. Even if the surface electric field strength is orders of magnitude lower, we still observe a notable photocarrier extraction rate under higher reverse bias. Clearly, this is a different observation compared to the strong surface electric field in the

devices (~10^6 V/m; Fig. 4, A to D). With increasing reverse bias, the EQE at the long wavelength saturates first, while the EQE at the short wavelength of ~475 nm does not approach unity even under high applied voltages. This condition implies a much higher surface potential (summarized in Fig. 3I) with several volts of applied voltage, while the short-wavelength photocarrier collection still fails to saturate, suggesting that the surface potential–induced change in surface defects is not the major reason for photocarrier extraction. In addition, these long wavelength–generated photocarriers can also be fully collected without a strong surface electric field. This indicates that the high kinetic energy of the hot photocarriers approaching the surface is a key reason why these photocarriers can overcome the surface recombination process. Most of the photocarriers below 1000-nm wavelength are generated within the depletion region (simulated in Fig. 3H). For the photocarriers generated at longer wavelengths, the longer drift distance under the electric field enables a higher velocity (the velocity is perpendicular to the collecting surface) and, thus, higher kinetic energy when they reach the surface. The high kinetic energy of these photocarriers contributes to largely overcoming the surface recombination processes. This explanation is consistent with the following observations pertaining to Fig. 4E, when the wavelength is below 1010 nm: (i) The long-wavelength EQE has a generally higher value than the short-wavelength EQE when the applied voltage is below −0.3 V, even if the sample has a lower absorption at a longer wavelength. (ii) The long-wavelength EQE saturates first with increased applied bias. (iii) The short-wavelength EQE needs a much larger applied bias to saturate or may not even saturate, meaning that the photocarriers generated at these near-surface regions cannot acquire sufficient potential energy even under the influence of high applied bias.

This is further confirmed by the calculated IQE in Fig. 4F. The long-wavelength photocarriers (generated far inside the silicon absorber) saturate to near-unity IQE first, demonstrating more than ~99% IQE from 510 to 975 nm at −4 V. Meanwhile, the short-wavelength photocarriers (generated near the surface) are not completely collected under high reverse bias. Also, comparing the devices in Fig. 4 (A and C), it is concluded that photocarriers acquiring sufficient kinetic energy can overcome the trap-assisted surface recombination process even in the absence of a strong near-surface electric field. This conclusion provides potential guidance in designing multifunctional optoelectronic devices. For example, at −0.1 V bias, the EQE peaks at ~1010-nm wavelength in Fig. 4E, suggesting great potential in producing a narrowband photodetector by using surface recombination as a natural filter (56, 57). To better show the details of the high-value EQE/IQE results, zoomed-in images for Fig. 4 (E and F) are plotted in fig. S13.

The EQE under a high reverse bias of −4 V (device in Fig. 4E) is compared with the EQE for an annealed device at 0 V in fig. S14 (58). For the unannealed devices in this work, there is a limited chemical passivation effect at the surface, while the annealed device shows excellent surface chemical passivation (58). In our previous work, it is demonstrated that a wide depletion region and a well chemically passivated surface enable a nearly complete collection of broadband photocarriers at 0 V bias (58). With a nearly constant optical generation profile, the unannealed device in this work under a large reverse bias (red curve in fig. S14) indicates an almost-constant long-wavelength EQE compared with the results of the well-passivated devices at 0 V bias (black curve in fig. S14). This

implies that the photocurrent gain effect is mostly mitigated for the low-doped Si (1.5×10^{12} cm^{-3} doping level) device in this work. The Fermi level of the ITO thin film lies in the middle region of the Si forbidden band, inducing a wide depletion region and hence making it hard for charge carrier tunneling at large reverse bias, which in turn hinders the photocarrier recycling process. It is suggested that with a definitive low surface defect density, all these photocarriers can be collected at 0 V bias via the combination of field effect contact and chemical passivation—evident from the almost identical long-wavelength EQE in these two devices with/without surface passivation. To further consolidate the results, another device with 1.9×10^{16} cm^{-3} doping level is characterized in fig. S15. The simulated photocurrent under 1 sun for all devices is given in fig. S16.

Light-trapping Si device characterization

The foregoing device constructs on planar silicon are now extended to silicon devices with surface light-trapping topologies in Fig. 5, where we observe a consistency in device performance. A photograph illustrating wafer-scale fabricated photonic crystals (PhCs) is shown in Fig. 5A. Note that these PhCs with nanometer-width mesa were realized by a conventional industry-compatible photolithography process. An optical photograph of a device being tested is shown as an inset in Fig. 5A, where light is focused onto the active region of the device with integrated PhCs. A scanning electron microscopy (SEM) image for the PhCs is given in Fig. 5B. These PhCs are composed of periodic inverted pyramids exhibiting an ~3 μm base width with mesas of tens of nanometers in size. A high level of evenness of the nanometer mesa width over a large area of the sample is observed. The high-resolution transmission electron microscopy (HRTEM) image for a single ITO-coated PhC is shown in Fig. 5C. The smooth ITO thin films covering the entire surface of the PhC are examined. The mesa width is confirmed to be within ~100 nm. Notably, a conformal native oxide is observed attaching the whole surface of the pyramid. This is further confirmed in HRTEM images for the sidewall and corner regions of the PhC (fig. S17). The thickness of the native oxide is measured to be ~1.8 nm checking the corner region of the mesa. For these PhCs, this oxide is naturally grown in air, which helps to maintain the original surface states of the sample. Additional electron microscopy characterizations, which include PhCs with various lattice constants, cross-sectional SEM images, and EDS mapping results, are given in figs. S18 to S20.

The details of the optical properties of PhCs are described elsewhere (59, 60). The optical properties of the uncoated PhCs with various lattice constants from 4 to 12 μm are measured in fig. S21. The spectral transmission, reflection, and absorption profiles of ITO/Si PhCs (3 μm lattice constant) are shown in Fig. 5D. High absorption on average of more than ~90% from 300 to 1000 nm is observed. An n-Si wafer with 3000 ohm·cm resistivity is used to configure the device, the EQE of which is measured in Fig. 5E. No O_2 is flowed during ITO sputtering for this device. The EQE saturates at a certain level under a high applied voltage. The structure exhibits a high broadband EQE under a high reverse bias: More than ~90% EQE from 435- to 980-nm wavelengths is observed under −8 V bias, demonstrating an excellent photocarrier collection rate with a tunable surface potential.

The EQE at −8 V is compared with the optical absorption for devices with/without Al back reflector in Fig. 5F. There is short-
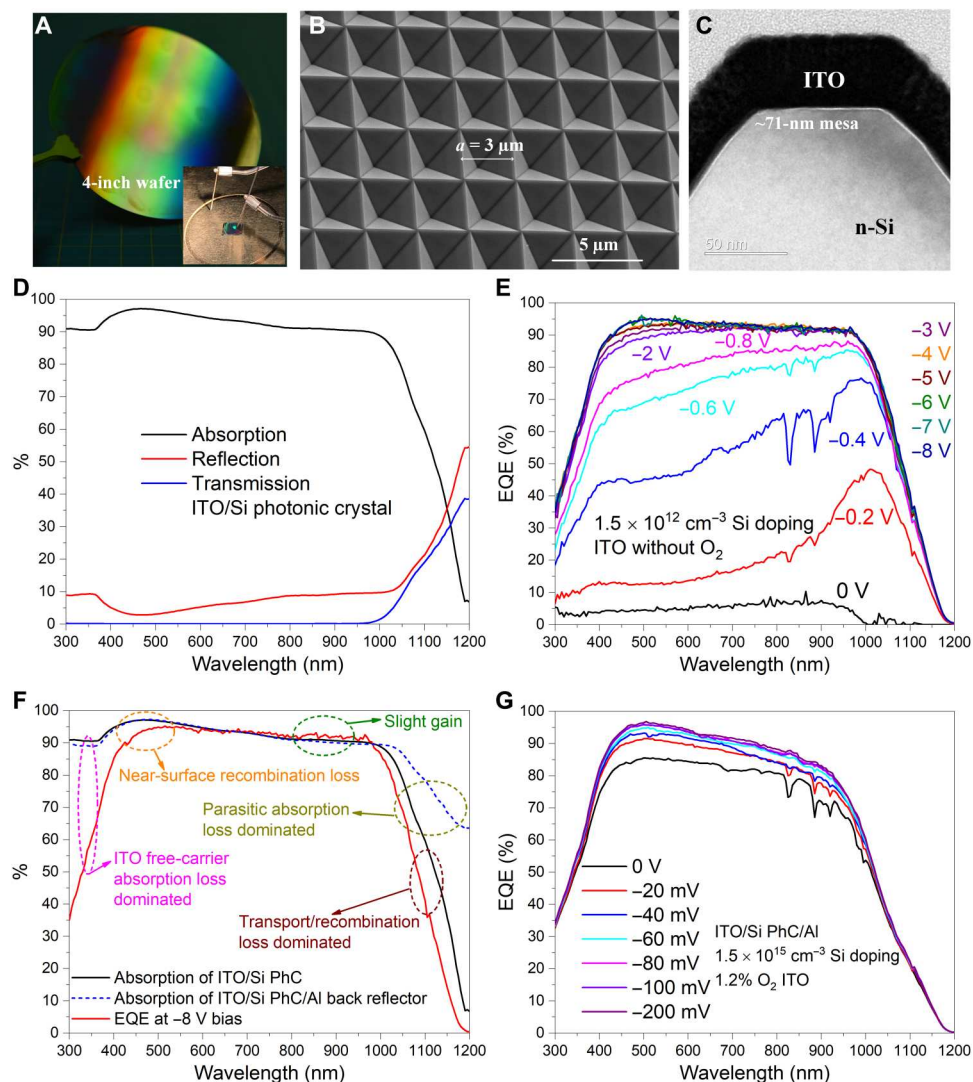
Fig. 5. Characterization of the devices with light-trapping surface topologies. (**A**) An optical photograph indicating the large area of photonic crystals (PhCs) onto a 4-inch wafer, including an inset of an optical photograph of a test device. (**B**) Top-view scanning electron microscopy (SEM) image of as-fabricated wave interference PhCs with 3 μm lattice constant. (**C**) High-resolution transmission electron microscopy (HRTEM) image for the mesa region of ITO-coated PhC. (**D**) Absorption, reflection, and transmission profiles of the ITO/PhC on Si structure. (**E**) EQE under different reverse voltage biases for ITO-coated PhC on a high-resistivity wafer (3000 ohm·cm, 1.5×10^{12} cm^{-3} doping concentration). (**F**) Comparison between the optical absorption and EQE under −8 V bias. (**G**) EQE under different small reverse biases for ITO-coated (1.2% O$_2$ flow) PhC on a low-resistivity wafer (3 ohm·cm, 1.5×10^{15} cm^{-3} doping concentration).

wavelength EQE loss, e.g., ~91% total absorption is obtained at 300-nm wavelength; however, the EQE is only ~35% under −8 V bias at the same wavelength. This portion of loss is dominated by the free-carrier absorption in the ITO thin film. The absorption peaks at 450 nm with a value of ~97%, while the EQE is only ~90% at this wavelength, which is mainly due to surface recombination loss for short-wavelength photogeneration. We assume that even under a high applied bias of −8 V, some near surface–generated photocarriers still cannot completely overcome the surface recombination process due to the lower (by order of magnitude) near-surface electric field for the 3000 ohm·cm Si device. The EQE is ~1 to ~2% higher than the absorption rate from 700 to 1000 nm, attributed to the photocurrent gain effect under a high electric field. The EQE is slightly lower than the optical absorption (black curve,

without Al back reflector) from 1000 to 1200 nm, due to the transport loss of these long wavelength–generated photocarriers (i.e., these photocarriers may recombine due to either the long transport distance or the unoptimized back surface). Compared with the entire optical absorption of the ITO/Si PhCs/Al back-reflector structure (blue dashed line in Fig. 5F), the proposed photocarrier extraction experiment in this work clearly shows that a substantial fraction of the "observed optical absorption" cannot truly contribute to the real photogeneration for a certain light-trapping design. For example, at 1200-nm wavelength in Fig. 5F, we observe ~65% optical absorption (blue dashed line), while the EQE is only ~1%. The IQE at −8 V is calculated in fig. S22, where near-100% IQE is observed over a broadband of wavelengths, suggesting that nearly all photocarriers across the optical absorber are collected with limited

gain effect. This limited photocurrent gain effect indicates that the experiment proposed in this work can be potentially used to estimate the real photogeneration rate for all optical absorbers with various light-trapping designs and materials. For instance, it is sometimes difficult to ascertain the real optical absorption and the resulting photogeneration in an optical absorber. Possible reasons include the free-carrier absorption in conductors or even that due to the defect levels and initial doping of semiconductor causing additional optical absorption, which cannot really contribute to collectable photocarriers. The experimental results in this work provide an approach to resolve this problem—collecting nearly all measurable photocarriers. Under a wide depletion region and a proper surface electric field distribution, broadband-generated photocarriers are nearly completely collected with limited gain effect, as shown in Fig. 5E. Thus, the ratio of collected photocarriers to absorbed photons provides a valid balanced estimate of the real photogeneration in an absorber. The photocurrent versus reverse applied voltage is simulated in fig. S23.

Another strong surface electric field device with ITO deposition (at 1.2% O_2 flow) onto PhCs integrated on n-Si (400 μm thickness, 3 ohm·cm) is characterized in Fig. 5G. Unlike the planar device operating at 0 V bias (Fig. 4A), an additional −100 mV is required to saturate the EQE. A high EQE of >~96% from 470- to 535-nm wavelength is observed for this device, confirming the assumption that there exists near-surface recombination loss for devices in Fig. 5F due to the lower surface electric field. Note that the Si surface states may vary after processing [for example, PhC fabrication, random surface texturing, and the Radio Corporation of America (RCA) cleaning]—considering that maintaining an absolutely constant surface state for all the fabrication processes (compared with the untreated Si surface in Fig. 4) is technically quite challenging. The randomly textured sample is characterized in fig. S24.

Theoretical simulation

Theoretical simulation results are presented in Fig. 6 to better understand the photo response of the devices studied in this work. 3D finite-difference time-domain (FDTD) simulations of the photon electric field distribution under two illumination wavelengths (450 and 750 nm) are shown in Fig. 6A. For 450 nm, most of the optical field is distributed within a 1-μm distance from the top surface for these PhCs. The optical simulation for 550- and 650-nm wavelengths is given in fig. S25. A similar near-surface optical field distribution is observed under 550-nm illumination, indicating predominant photogeneration in the near surface—correlating with the short wavelength–associated photocarrier collection with sufficiently high near-surface electric field strength. At longer wavelengths (650 and 750 nm), the optical electric field intensity extends to greater depth in the Si wafer—this indicates that a combination of both diffusion and drift transport processes will be involved in photocarrier collection at these wavelengths for narrow depletion region devices as simulated in Fig. 6B. The electric field and electric potential distributions at −1 V bias for an n-Si device with 3 ohm·cm resistivity are simulated in Fig. 6B, using 2D finite element analysis (FEA) modeling. The simulations from 0 V to −0.8 V bias are given in fig. S26. The simulated strong near-surface electric field (greater than 10^6 V/m) accounts for the ultrahigh peak EQE (~97% at 500 nm) for the 3 ohm·cm device in Fig. 5G.

The energy band for high-resistivity Si device (3000 ohm·cm) is simulated in Fig. 6C. A wide depletion region with tens of micrometers width is further evident for this device. Assuming that there is no scattering process, the potential energy U of a generated photocarrier is converted to its kinetic energy during the low electric field transport process. Thus, the maximum kinetic energy that a photocarrier can acquire is dependent on its generation position. For these photocarriers generated within the depletion region, they have a potential energy gradient wherein photocarriers generated closer to the collecting surface have a lower potential energy (labeled as U_{950nm} to U_{600nm}; the generation position is roughly estimated by the Si absorption depth for each wavelength). The EQE is then influenced by the wavelength-dependent photocarrier absorption rate and generation location. The potential energy gradient at different wavelengths of photogeneration explains the observations in Figs. 4E and 5E: With increasing applied bias, the long-wavelength EQE saturates first, while the long-wavelength EQE is generally higher than the short-wavelength EQE at small biases. The electric potential difference between the position where photocarriers are generated and the collecting surface is thus a key reason why photocarriers overcome the unpassivated surface, well explaining the observed EQE/IQE results. Hot photocarriers acquiring sufficiently high kinetic energy can completely overcome the surface trap-assisted recombination for nearly 100% extraction. Note that the case considering the lattice scattering or photocarrier interaction would be rather complicated wherein the practical kinetic energy distribution profile is a function of the spatial location of photon absorption, electric field distribution, and phonon/carrier scattering processes during transport, which we leave as an open issue for subsequent research.

The energy band for narrow depletion region devices, simulated in Fig. 6D, explains the results in Fig. 4 (A to D). For these devices, photocarriers are predominantly generated outside of the depletion region, and hence, the maximum kinetic energy that the carriers can acquire when approaching the surface depends on the surface potential. This surface potential is constant for all photocarriers generated outside of the depletion region, substantiating the nearly constant broadband IQEs observed for all devices with narrow depletion regions [from 450- to 800-nm wavelength, shown in Fig. 4 (B and D) and figs. S15C and S24D]. This also explains the strong surface electric field effect on effective near surface–generated photocarrier collection, as observed in Figs. 4A and 5G. The strong near-surface electric field creates a large electric potential at the position where these short-wavelength photocarriers are generated, thus enabling nearly complete photocarrier collection.

DISCUSSION

A surface Haynes-Shockley experiment is designed and carried out to analyze the loss of photogenerated carriers due to surface recombination and, in particular, to determine the influence of the near-surface electric field on photocarrier extraction via a simple tunable rectifying junction. For a typical silicon unpassivated surface, we experimentally establish that when the surface electric field approaches a sufficiently high strength, or the energy of photocarriers approaching the surface is appropriately high, almost all the photocarriers will be collected with little surface recombination loss. The experiments and supporting analysis demonstrate the viability of this approach to examine silicon surfaces with various light-trapping morphologies. The results herein provide a general framework to aid in the development of surface passivation, mitigation of
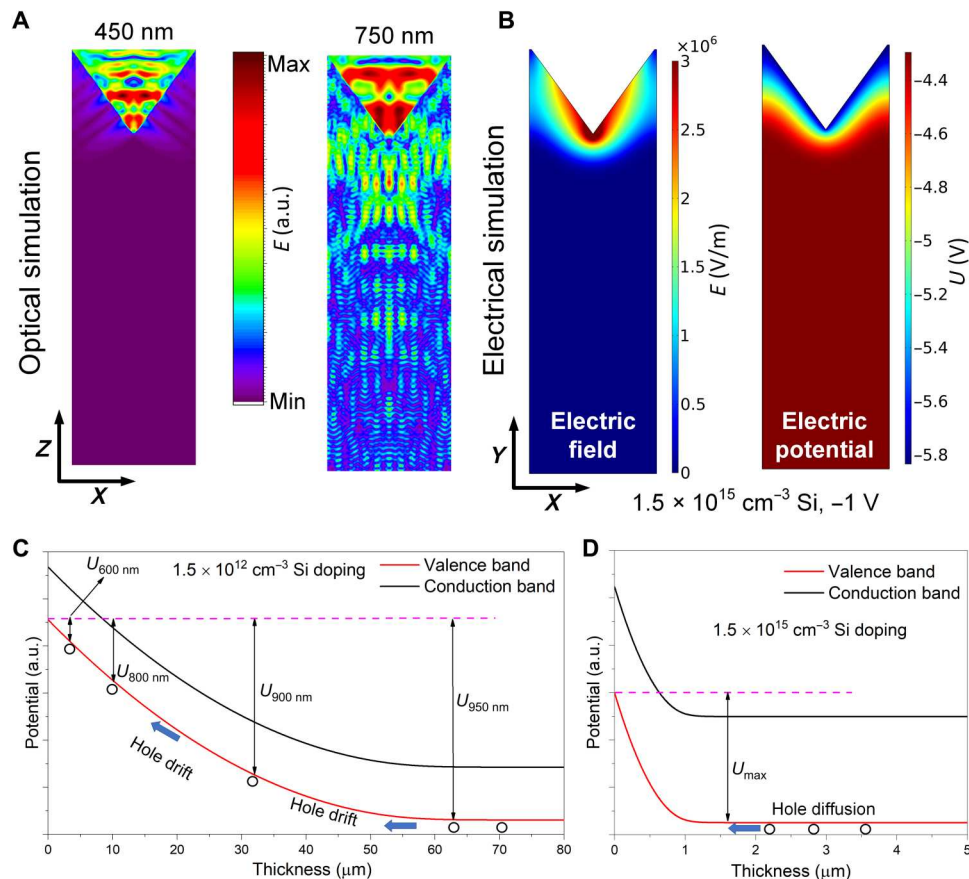
Fig. 6. Optical and electrical simulations. (**A**) Finite-difference time-domain (FDTD) simulations of the optical electric field distribution for PhCs under the illumination of 450- and 780-nm wavelengths. (**B**) 2D finite element analysis (FEA) simulations for electric field and electric potential distributions in a device integrated with PhCs. n-Si (3 ohm·cm) is used for simulation. The simulation areas for all figures in (A) and (B) are constant with 3 μm width × 10 μm length. (**C**) 1D FEA simulation of the energy band as a function of thickness for the biased n-Si device with a wide depletion region (3000 ohm·cm n-Si is used for simulation). (**D**) 1D FEA simulation of the energy band as a function of thickness for the biased n-Si device with a narrow depletion region (3 ohm·cm n-Si is used for simulation).

photocarrier recombination loss, and implementation of optimal light-trapping structures for the design and fabrication of high-performance optoelectrical devices, as well as determining the real photogeneration rate by collecting nearly all measurable photocarriers to establish the efficacy of various light-trapping designs.

MATERIALS AND METHODS
Random pyramid fabrication
The random pyramid fabrication was as follows: As-received Si wafers were dipped in 2% hydrofluoric acid (HF) for 2 min to remove the native oxide. Potassium hydroxide (KOH) and isopropyl alcohol were mixed with deionized water at a ratio of 4:5:91 as an etchant. The wafers were then dipped in the etchant for 20 min at 70°C to produce the random pyramids. An RCA cleaning process was conducted after random texturing.

PhC fabrication
The fabrication process for PhCs was as follows: First, 200-nm thermal oxide was grown on both sides of the wafers. Then, UV photolithography was used to pattern an array of square openings onto the oxide wafers. The samples were then dipped in buffered oxide etchant (BOE; 6:1) to etch the oxide all the way down to the Si surface. Subsequent anisotropic etching in KOH solution (30%) was conducted at 75°C to create inverse pyramid structures. Nanometer-scale mesas for adjacent inverse pyramids were realized by changing the etching time. After KOH etching, the thermal oxide was removed by another BOE dipping step.

ITO thin-film deposition
The sputtering chamber (Kurt J. Lesker) was pumped down to a pressure below 10^{-6} torr before every deposition. A shadow mask was used to define the contact region. A 30-min pre-sputtering was conducted before the sample deposition. During deposition, 100-SCCM (standard cubic centimeter per minute) gas flow with various Ar to O_2 ratios was applied. A 5-mtorr pressure and a 100-W radio frequency (RF) power were set for deposition at room temperature. A quartz monitor was used to record a constant deposition thickness for all devices.

Device fabrication
All Si wafers used in this work are n-type phosphorus doped, <100> orientation, and double-side polished. For Si wafers with ~3 ohm·cm resistivity, devices in Fig. 5G explored Czochralski (CZ)

Si with 400 μm thickness, while all the other devices explored float zone (FZ) Si with 290 μm thickness. The ~3000 ohm·cm wafer is FZ Si with 400 μm thickness. The ~0.3 ohm·cm wafer is CZ Si with 200 μm thickness. The device fabrication process began with 4-inch wafers. Two different surface morphologies were investigated. The first set of samples was "as-received" wafers, where the native oxide was kept without any surface treatment to maintain the original Si surface states. The second set of samples was integrated with random pyramid and wave interference PhC light-trapping structures, for which native SiO_x growth was conducted by exposing samples to air before ITO deposition. ITO thin film with various O_2 flow ratios was deposited as a top rectifying contact, and ~300-nm Al was deposited on the backside of the sample to form an ohmic contact. No posttreatment was conducted after Al deposition.

Device surface and material characterization

SEM characterizations in Fig. 5B and fig. S18 were performed by a Q250FEG SEM. SEM images in fig. S20 were taken by Hitachi SU-8230. The HRTEM images were taken by Hitachi HF-3300. The surface morphology for ITO thin films and random pyramids was measured by Dimension Icon AFM (Bruker). The work function and the resistivity/carrier concentration of ITO thin films were determined by UPS (Thermo Fisher Scientific) and a Hall effect system (Nanometrics), respectively.

Optical characterization

The reflection, transmission, and absorption were measured with a UV-Vis spectrometer (Lambda PerkinElmer 1050). ITO thin films were deposited on a quartz substrate for transmission measurement.

Optoelectronic characterization

Current-voltage and capacitance-voltage properties were determined by a semiconductor analyzer (Keithley, 4200) with samples fixed onto a shielded probe station (MPI Corporation). The EQE was measured by a QE-R system (Enlitech).

Optical simulation

A 3D FDTD simulation was conducted using a commercial software (Lumerical FDTD). A proper meshing rate was set to balance the simulation load and accuracy. The perfectly matched layer boundary condition was set for the vertical z direction, while periodic boundaries were set for the x and y directions. A plane light source was used for illumination. The 2D cross-sectional distribution of the electric field was obtained for various wavelength illuminations.

Electrical simulation

The electric field distribution under various applied voltages was determined by 1D and 2D FEA simulations (semiconductor physics module, COMSOL Multiphysics).

Supplementary Materials

This PDF file includes:
Supplementary Text
Figs. S1 to S26
References

REFERENCES AND NOTES

1. P. G. O'Brien, K. K. Ghuman, A. A. Jelle, A. Sandhel, T. E. Wood, J. Y. Y. Loh, J. Jia, D. Perovic, C. V. Singh, N. P. Kherani, C. A. Mims, G. A. Ozin, Enhanced photothermal reduction of gaseous CO_2 over silicon photonic crystal supported ruthenium at ambient temperature. *Energ. Environ. Sci.* **11**, 3443–3451 (2018).

2. M. Ghoussoub, M. Xia, P. N. Duchesne, D. Segal, G. Ozin, Principles of photothermal gas-phase heterogeneous CO_2 catalysis. *Energ. Environ. Sci.* **12**, 1122–1142 (2019).

3. K. K. Ghuman, L. B. Hoch, P. Szymanski, J. Y. Loh, N. P. Kherani, M. A. El-Sayed, G. A. Ozin, C. V. Singh, Photoexcited surface frustrated Lewis pairs for heterogeneous photocatalytic CO_2 reduction. *J. Am. Chem. Soc.* **138**, 1206–1214 (2016).

4. A. Richter, R. Müller, J. Benick, F. Feldmann, B. Steinhauser, C. Reichel, A. Fell, M. Bivour, M. Hermle, S. W. Glunz, Design rules for high-efficiency both-sides-contacted silicon solar cells with balanced charge carrier transport and recombination losses. *Nat. Energy* **6**, 429–438 (2021).

5. W. Liu, J. Shi, L. Zhang, A. Han, S. Huang, X. Li, J. Peng, Y. Yang, Y. Gao, J. Yu, K. Jiang, X. Yang, Z. Li, W. Zhao, J. Du, X. Song, J. Yin, J. Wang, Y. Yu, Q. Shi, Z. Ma, H. Zhang, J. Ling, L. Xu, J. Kang, F. Xu, J. Liu, H. Liu, Y. Xie, F. Meng, S. De Wolf, F. Laquai, Z. Di, Z. Liu, Light-induced activation of boron doping in hydrogenated amorphous silicon for over 25% efficiency silicon solar cells. *Nat. Energy* **7**, 427–437 (2022).

6. I. Massiot, A. Cattoni, S. Collin, Progress and prospects for ultrathin solar cells. *Nat. Energy* **5**, 959–972 (2020).

7. M. Köhler, M. Pomaska, P. Procel, R. Santbergen, A. Zamchiy, B. Macco, A. Lambertz, W. Duan, P. Cao, B. Klingebiel, S. Li, A. Eberst, M. Luysberg, K. Qiu, O. Isabella, F. Finger, T. Kirchartz, U. Rau, K. Ding, A silicon carbide-based highly transparent passivating contact for crystalline silicon solar cells approaching efficiencies of 24%. *Nat. Energy* **6**, 529–537 (2021).

8. J. Heinonen, A. Haarahiltunen, M. Dov Serue, V. Vähänissi, T. P. Pasanen, H. Savin, L. Werner, M. A. Juntunen, High-sensitivity NIR photodiodes using black silicon. *Proc. SPIE* **11276**, 112760G (2020).

9. J. Heinonen, A. Haarahiltunen, V. Vähänissi, T. P. Pasanen, H. Savin, M. A. Juntunen, Effect of anode sheet resistance on rise time of black silicon induced junction photodiodes. *Proc. SPIE* **11997**, 119970C (2022).

10. M. Garin, J. Heinonen, L. Werner, T. P. Pasanen, V. Vahanissi, A. Haarahiltunen, M. A. Juntunen, H. Savin, Black-silicon ultraviolet photodiodes achieve external quantum efficiency above 130%. *Phys. Rev. Lett.* **125**, 117702 (2020).

11. C. Fuentes-Hernandez, W. F. Chou, T. M. Khan, L. Diniz, J. Lukens, F. A. Larrain, V. A. Rodriguez-Toro, B. Kippelen, Large-area low-noise flexible organic photodiodes for detecting faint visible light. *Science* **370**, 698–701 (2020).

12. M. A. Juntunen, J. Heinonen, V. Vähänissi, P. Repo, D. Valluru, H. Savin, Near-unity quantum efficiency of broadband black silicon photodiodes with an induced junction. *Nat. Photonics* **10**, 777–781 (2016).

13. Z. Li, X. Liu, C. Zuo, W. Yang, X. Fang, Supersaturation-controlled growth of monolithically integrated lead-free halide perovskite single-crystalline thin film for high-sensitivity photodetectors. *Adv. Mater.* **33**, e2103010 (2021).

14. W. Song, J. Chen, Z. Li, X. Fang, Self-powered MXene/GaN van der waals heterojunction ultraviolet photodiodes with superhigh efficiency and stable current outputs. *Adv. Mater.* **33**, e2101059 (2021).

15. W. Ouyang, F. Teng, J.-H. He, X. Fang, Enhancing the photoelectric performance of photodetectors based on metal oxide semiconductors by charge-carrier engineering. *Adv. Funct. Mater.* **29**, 1807672 (2019).

16. M. Portnoi, P. A. Haigh, T. J. Macdonald, F. Ambroz, I. P. Parkin, I. Darwazeh, I. Papakonstantinou, Bandwidth limits of luminescent solar concentrators as detectors in free-space optical communication systems. *Light. Sci. Appl.* **10**, 3 (2021).

17. Q. Shan, C. Wei, Y. Jiang, J. Song, Y. Zou, L. Xu, T. Fang, T. Wang, Y. Dong, J. Liu, B. Han, F. Zhang, J. Chen, Y. Wang, H. Zeng, Perovskite light-emitting/detecting bifunctional fibres for wearable LiFi communication. *Light. Sci. Appl.* **9**, 163 (2020).

18. C. Bao, C. Xu, J. Yang, S. Bai, P. Teng, Y. Yang, J. Wang, N. Zhao, W. Zhang, W. Huang, F. Gao, Bidirectional optical signal transmission between two identical devices using perovskite diodes. *Nat. Electron.* **3**, 156–164 (2020).

19. H. Fang, C. Zheng, L. Wu, Y. Li, J. Cai, M. Hu, X. Fang, R. Ma, Q. Wang, H. Wang, Solution-processed self-powered transparent ultraviolet photodetectors with ultrafast response speed for high-performance communication system. *Adv. Funct. Mater.* **29**, 1809013 (2019).

20. K. Yoshikawa, H. Kawasaki, W. Yoshida, T. Irie, K. Konishi, K. Nakano, T. Uto, D. Adachi, M. Kanematsu, H. Uzu, K. Yamamoto, Silicon heterojunction solar cell with interdigitated back contacts for a photoconversion efficiency over 26%. *Nat. Energy* **2**, 17032 (2017).

21. A. Tomasi, B. Paviet-Salomon, Q. Jeangros, J. Haschke, G. Christmann, L. Barraud, A. Descoeudres, J. P. Seif, S. Nicolay, M. Despeisse, S. De Wolf, C. Ballif, Simple processing of

22. M. T. Greiner, L. Chai, M. G. Helander, W. M. Tang, Z. H. Lu, Metal/metal-oxide interfaces: How metal contacts affect the work function and band structure of MoO₃. *Adv. Funct. Mater.* **23**, 215–226 (2013).

23. M. T. Greiner, M. G. Helander, W. M. Tang, Z. B. Wang, J. Qiu, Z. H. Lu, Universal energy-level alignment of molecules on metal oxides. *Nat. Mater.* **11**, 76–81 (2011).

24. P. Mahtani, K. R. Leong, B. Jovet, D. Yeghikyan, N. P. Kherani, High quality amorphous–crystalline silicon heterostructure prepared by grid-biased remote radio-frequency plasma enhanced chemical vapor deposition. *J. Non Cryst. Solids* **358**, 3396–3402 (2012).

25. L. Serenelli, R. Chierchia, M. Izzi, M. Tucci, L. Martini, D. Caputo, R. Asquini, G. de Cesare, Hydrogen plasma and thermal annealing treatments on a-Si:H thin film for c-Si surface passivation. *Energy Procedia* **60**, 102–108 (2014).

26. J. L. Benton, C. J. Doherty, S. D. Ferris, D. L. Flamm, L. C. Kimerling, H. J. Leamy, Hydrogen passivation of point defects in silicon. *Appl. Phys. Lett.* **36**, 670–671 (1980).

27. J. Zhao, A. Wang, M. A. Green, F. Ferrazza, 19.8% efficient "honeycomb" textured multi-crystalline and 24.4% monocrystalline silicon solar cells. *Appl. Phys. Lett.* **73**, 1991–1993 (1998).

28. A. W. Blakers, A. Wang, A. M. Milne, J. Zhao, M. A. Green, 22.8% efficient silicon solar cell. *Appl. Phys. Lett.* **55**, 1363–1365 (1989).

29. H. Savin, P. Repo, G. von Gastrow, P. Ortega, E. Calle, M. Garin, R. Alcubilla, Black silicon solar cells with interdigitated back-contacts achieve 22.1% efficiency. *Nat. Nanotechnol.* **10**, 624–628 (2015).

30. T. G. Allen, J. Bullock, X. Yang, A. Javey, S. De Wolf, Passivating contacts for crystalline silicon solar cells. *Nat. Energy* **4**, 914–928 (2019).

31. J. Bullock, M. Hettick, J. Geissbühler, A. J. Ong, T. Allen, C. M. Sutter-Fella, T. Chen, H. Ota, E. W. Schaler, S. De Wolf, C. Ballif, A. Cuevas, A. Javey, Efficient silicon solar cells with dopant-free asymmetric heterocontacts. *Nat. Energy* **1**, 15031 (2016).

32. A. Ingenito, G. Nogay, Q. Jeangros, E. Rucavado, C. Allebé, S. Eswara, N. Valle, T. Wirtz, J. Horzel, T. Koida, M. Morales-Masis, M. Despeisse, F.-J. Haug, P. Löper, C. Ballif, A passiv-ating contact for silicon solar cells formed during a single firing thermal annealing. *Nat. Energy* **3**, 800–808 (2018).

33. X. Yang, W. Liu, M. De Bastiani, T. Allen, J. Kang, H. Xu, E. Aydin, L. Xu, Q. Bi, H. Dang, E. AlHabshi, K. Kotsovos, A. AlSaggaf, I. Gereige, Y. Wan, J. Peng, C. Samundsett, A. Cuevas, S. De Wolf, Dual-function electron-conductive, hole-blocking titanium nitride contacts for efficient silicon solar cells. *Joule* **3**, 1314–1327 (2019).

34. F. Wang, S. Zhao, B. Liu, Y. Li, Q. Ren, R. Du, N. Wang, C. Wei, X. Chen, G. Wang, B. Yan, Y. Zhao, X. Zhang, Silicon solar cells with bifacial metal oxides carrier selective layers. *Nano Energy* **39**, 437–443 (2017).

35. M. Xue, K. N. Nazif, L. Zheng, J. Jiang, C.-Y. Lu, N. Lee, K. Zang, Y. Chen, T. Zheng, T. I. Kamins, M. L. Brongersma, K. C. Saraswat, J. S. Harris, Free-standing 2.7 μm thick ultrathin crystalline silicon solar cell with efficiency above 12.0%. *Nano Energy* **70**, 104466 (2020).

36. M. Xue, R. Islam, A. C. Meng, Z. Lyu, C. Y. Lu, C. Tae, M. R. Braun, K. Zang, P. C. McIntyre, T. I. Kamins, K. C. Saraswat, J. S. Harris, Contact selectivity engineering in a 2 μm thick ul-trathin c-Si solar cell using transition-metal oxides achieving an efficiency of 10.8%. *ACS Appl. Mater. Interfaces* **9**, 41863–41870 (2017).

37. J. R. Haynes, W. Shockley, The mobility and life of injected holes and electrons in ger-manium. *Phys. Rev.* **81**, 835–843 (1951).

38. Y. Wan, C. Samundsett, J. Bullock, M. Hettick, T. Allen, D. Yan, J. Peng, Y. Wu, J. Cui, A. Javey, A. Cuevas, Conductive and stable magnesium oxide electron-selective contacts for efficient silicon solar cells. *Adv. Energy Mater.* **7**, 1601863 (2017).

39. J. Bullock, P. Zheng, Q. Jeangros, M. Tosun, M. Hettick, C. M. Sutter-Fella, Y. Wan, T. Allen, D. Yan, D. Macdonald, S. De Wolf, A. Hessler-Wyser, A. Cuevas, A. Javey, Lithium fluoride based electron contacts for high efficiency n-type crystalline silicon solar cells. *Adv. Energy Mater.* **6**, 1600241 (2016).

40. T. G. Allen, J. Bullock, Q. Jeangros, C. Samundsett, Y. Wan, J. Cui, A. Hessler-Wyser, S. De Wolf, A. Javey, A. Cuevas, A low resistance calcium/reduced titania passivated contact for high efficiency crystalline silicon solar cells. *Adv. Energy Mater.* **7**, 1602606 (2017).

41. Y. Ren, P. Liu, R. Liu, Y. Wang, Y. Wei, L. Jin, G. Zhao, The key of ITO films with high trans-parency and conductivity: Grain size and surface chemical composition. *J. Alloys Compd.* **893**, 162304 (2022).

42. J. F. Wager, D. A. Keszler, R. E. Presley, *Transparent Electronics* (Springer New York, 2008).

43. Y. J. Kim, S. B. Jin, S. I. Kim, Y. S. Choi, I. S. Choi, J. G. Han, Effect of oxygen flow rate on ITO thin films deposited by facing targets sputtering. *Thin Solid Films* **518**, 6241–6244 (2010).

44. K.-P. Kim, A. M. Hussain, D.-K. Hwang, S.-H. Woo, H.-K. Lyu, S.-H. Baek, Y. Jang, J.-H. Kim, Work function modification of indium–tin oxide by surface plasma treatments using different gases. *Jpn. J. Appl. Phys.* **48**, 021601 (2009).

45. S. Y. Kim, K. Hong, J.-L. Lee, K. H. Choi, K. H. Song, K. C. Ahn, Enhancement of physical properties of indium tin oxide deposited by super density arc plasma ion plating by O₂ plasma treatment. *Solid State Electron.* **52**, 1–6 (2008).

46. S. Li, M. Tian, Q. Gao, M. Wang, T. Li, Q. Hu, X. Li, Y. Wu, Nanometre-thin indium tin oxide for advanced high-performance electronics. *Nat. Mater.* **18**, 1091–1097 (2019).

47. S. K. Cheung, N. W. Cheung, Extraction of Schottky diode parameters from forward current-voltage characteristics. *Appl. Phys. Lett.* **49**, 85–87 (1986).

48. H. Altuntaş, Ş. Altındal, S. Özçelik, H. Shtrikman, Electrical characteristics of Au/n-GaAs Schottky barrier diodes with and without *SiO₂* insulator layer at room temperature. *Vacuum* **83**, 1060–1065 (2009).

49. Ş. Karataş, A. Türüt, The determination of electronic and interface state density distribu-tions of Au/n-type GaAs Schottky barrier diodes. *Phys. B Condens. Matter.* **381**, 199–203 (2006).

50. D. Mikulik, A. C. Meng, R. Berrazouane, J. Stückelberger, P. Romero-Gomez, K. Tang, F.-J. Haug, A. Fontcuberta i Morral, P. C. McIntyre, Surface defect passivation of silicon mi-cropillars. *Adv. Mater. Interfaces* **5**, 1800865 (2018).

51. P. S. Ho, E. S. Yang, H. L. Evans, X. Wu, Electronic states at silicide-silicon interfaces. *Phys. Rev. Lett.* **56**, 177–180 (1986).

52. A. Sharma, S. Yadav, P. Kumar, S. Ray Chaudhuri, S. Ghosh, Defect states and their energetic position and distribution in organic molecular semiconductors. *Appl. Phys. Lett.* **102**, 143301 (2013).

53. S. E. Meftah, M. Benhaliliba, M. Kaleli, C. E. Benouis, C. A. Yavru, A. B. Bayram, Optical and electrical characterization of thin film MSP heterojunction based on organic material Al/p-Si/P3HT/Ag. *Phys. B Condens. Matter.* **593**, 412238 (2020).

54. D. C. Tripathi, K. S. Rao, Y. N. Mohapatra, Impact of defect states on the capacitance voltage characteristics of space charge limited organic diodes, and determination of defect states. *J. Mater. Chem. C* **9**, 4903–4909 (2021).

55. X. Qiu, X. Yu, S. Yuan, Y. Gao, X. Liu, Y. Xu, D. Yang, Trap assisted bulk silicon photodetector with high photoconductive gain, low noise, and fast response by Ag hyperdoping. *Adv. Opt. Mater.* **6**, 1700638 (2018).

56. Y. Fang, Q. Dong, Y. Shao, Y. Yuan, J. Huang, Highly narrowband perovskite single-crystal photodetectors enabled by surface-charge recombination. *Nat. Photonics* **9**, 679–686 (2015).

57. Q. Lin, A. Armin, P. L. Burn, P. Meredith, Filterless narrowband visible photodetectors. *Nat. Photonics* **9**, 687–694 (2015).

58. Y. Zhang, J. Y. Y. Loh, N. P. Kherani, Facilely achieved self-biased black silicon heterojunction photodiode with broadband quantum efficiency approaching 100%. *Adv. Sci.* **9**, 2203234 (2022).

59. S. Bhattacharya, S. John, Beyond 30% conversion efficiency in silicon solar cells: A nu-merical demonstration. *Sci. Rep.* **9**, 12482 (2019).

60. S. Bhattacharya, I. Baydoun, M. Lin, S. John, Towards 30% power conversion efficiency in thin-silicon photonic-crystal solar cells. *Phys. Rev. Appl.* **11**, 014005 (2019).

61. B. L. Sharma, *Metal-Semiconductor Schottky Barrier Junctions and Their Applications* (Springer New York, 1984).